T_1 and T_2 Dual-Mode MRI Contrast Agent for Enhancing Accuracy by Engineered Nanomaterials

Tae-Hyun Shin,[†,∥] Jin-sil Choi,[†,∥] Seokhwan Yun,[‡] Il-Sun Kim,[‡] Ho-Taek Song,[§] Youngmee Kim,[⊥] Kook In Park,[‡,*] and Jinwoo Cheon[†,*]

[†]Center for Evolutionary Nanoparticles (CEN), Department of Chemistry, Yonsei University, Seoul 120-749, Korea, [‡]Department of Pediatrics and BK 21 and [§]Department of Radiology and Research Institute of Radiological Science, Yonsei University College of Medicine, Seoul 120-752, Korea, and [⊥]Department of Chemistry and Nano Science, Ewha Womans University, Seoul 120-750, Korea. [∥]T.-H.S. and J.-s.C. contributed equally.

ABSTRACT One of the holy grails in biomedical imaging technology is to achieve accurate imaging of biological targets. The development of sophisticated instrumentation and the use of contrast agents have improved the accuracy of biomedical imaging. However, the issue of false imaging remains a problem. Here, we developed a dual-mode artifact filtering nanoparticle imaging agent (AFIA) that comprises a combination of paramagnetic and superparamagnetic nanomaterials. This AFIA has the ability to perform "AND logic gate" algorithm to eliminate false errors (artifacts) from the raw images to enhance accuracy of the MRI. We confirm the artifact filtering capability of AFIA in MRI phantoms and further demonstrate that artifact-free imaging of stem cell migration is possible *in vivo*.

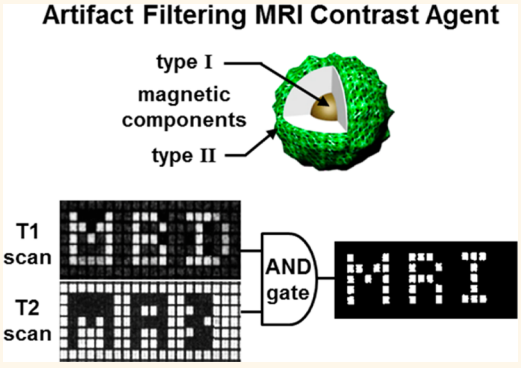

KEYWORDS: MRI contrast agent · magnetic nanoparticle · MRI · dual-mode contrast agent · stem cell tracking

Among various biomedical imaging modalities,[1−9] MRI is one of the most powerful tools because it can provide high-resolution anatomical images in a noninvasive manner.[10,11] In MRI, contrast agents are playing an increasingly important role to boost up imaging sensitivity by enhancing the contrast in regions of interest (ROI) with brighter or darker signals in T_1 or T_2 images.[12,13] This has led researchers to develop a variety of contrast agents.[13] In spite of such efforts, MRI images are often confronted with ambiguities derived from MRI artifacts.[14−16] The MRI artifacts, which originate from certain endogenous conditions, such as calcification, fat, hemorrhage, blood clot, and air, are problematic because they mimic MRI signals coming from contrast agents (Scheme 1).[15,16] There is frequent difficulty in discrimination between contrast agents and artifacts. The elimination of artifacts from MRI images is crucial to ensure accurate interpretation for the diagnosis.

Many attempts to overcome such obstacles can be found in the usages of modified MRI sequences or tailored contrast agents. Various MRI sequence techniques (*e.g.*, fat suppression, positive contrast technique) can enhance conspicuity of MRI images by suppressing artifacts through the resonant radio frequency tuning.[17,18] Even so, successful applications of such technique have still been confined to certain types of artifacts, and the complete elimination of artifacts has yet to be proven. Similarly, none of the dual-mode contrast agents have unambiguously demonstrated the ability to systematically eliminate artifacts from the images obtained from *in vitro* and *in vivo* systems.[19−22]

Herein, we demonstrate artifact filtering imaging agent (AFIA) that can eliminate the false errors in MRI imaging. In our previous study,[22] we introduced the primitive concept of dual-mode contrast agents, without suggesting their general usefulness nor efficacy for *in vivo* imaging. In this study, we report that the concept of AFIA can be generally operative with the use of a number of different magnetic nanomaterials. In addition, we establish the systematic T_1 and

* Address correspondence to kipark@yuhs.ac, jcheon@yonsei.ac.kr.

Received for review November 19, 2013 and accepted March 6, 2014.

Published online March 27, 2014
10.1021/nn405977t

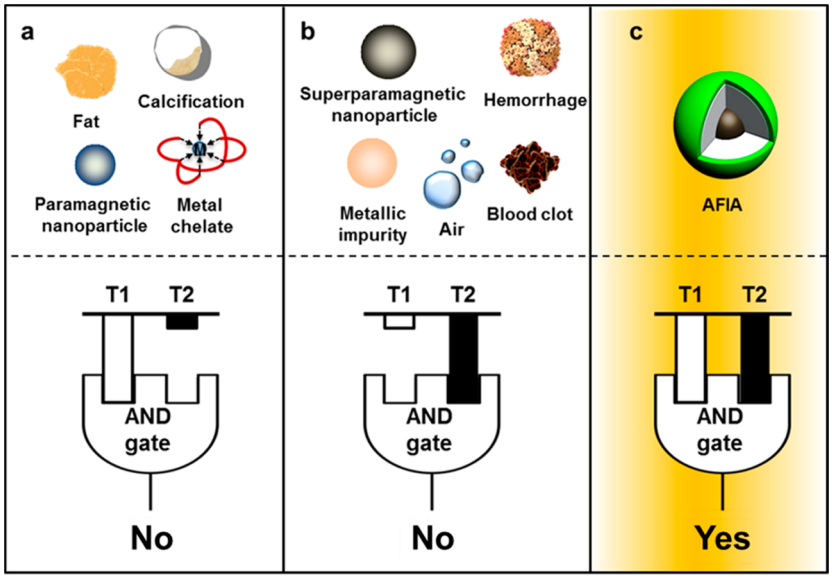

Scheme 1. Illustration of MRI artifact filtering imaging agent (AFIA) and the AND logic gate process. (a,b) Artifacts and typical contrast agents give high contrast effects in either T_1 or T_2 but do not satisfy AND logic. (c) AFIA can provide simultaneously strong T_1 and T_2 signals and fulfill AND logic.

T_2 imaging protocols to eliminate artifacts *via* "AND logic gate" process (Scheme 1c). By using Mn-MOF containing AFIA and AND logic algorithm, we successfully track stem cells *in vivo*.

RESULTS AND DISCUSSION

Design and Generalization of AFIA. AFIA has inorganic core–shell structure which is composed of a superparamagnetic nanoparticle (core), SiO_2 (separating layer), and paramagnetic material (shell) (Scheme 1c and Figure 1a). The superparamagnetic nanoparticle is located in the core because it can generate adequate magnetic field on the surrounding water molecules and accelerate the T_2 relaxation process.[12,13] On the other hand, paramagnetic material is positioned on the shell because T_1 relaxation of water molecules is strongly affected by the direct contact between water and paramagnetic materials.[12,13] By inserting a separating layer (SiO_2), which is rigid enough to maintain the distance between two magnetic materials, the magnetic coupling between the two materials can be controlled and simultaneously high T_1 and T_2 contrast effects can be achieved.[22] We observed that separating layer thickness of 16 nm is adequate to have high T_1 and T_2 signals.

In order to demonstrate the generality of our design concept, a variety of AFIAs are synthesized by using a combination of materials in the core and shell while fixing the thickness of the separating SiO_2 layer at 16 nm (Figure 1b). The superparamagnetic materials used for this purpose include Fe_3O_4 (15 nm), $CoFe_2O_4$ (15 nm), $MnFe_2O_4$ (15 nm), and $ZnFe_2O_4$ (15 nm), and the paramagnetic materials are $Gd_2O(CO_3)_2$, $Dy_2O(CO_3)_2$, $Eu_2O(CO_3)_2$, $Gd(BTC)(H_2O)$, and [ImH]-[$Mn(BTC)(H_2O)$] (BTC = 1,3,5-benzenetricarboxylate; ImH = protonated imidazole). All of the AFIAs, including Fe_3O_4@SiO_2@$Gd_2O(CO_3)_2$, $CoFe_2O_4$@SiO_2@$Gd_2O(CO_3)_2$, $CoFe_2O_4$@SiO_2@$Eu_2O(CO_3)_2$, $CoFe_2O_4$@SiO_2@$Dy_2O(CO_3)_2$, $MnFe_2O_4$@SiO_2@$Gd(BTC)(H_2O)$, $ZnFe_2O_4$@SiO_2@[ImH][$Mn(BTC)(H_2O)$], display concurrently high T_1 and T_2 contrast effects (Figure 1c).

Mn-MOF Containing AFIA (mAFIA) for Biological Application. Among various types of AFIAs, considering biocompatibility and high contrast effects, we choose Mn-MOF containing AFIA as the representative case study. mAFIA is composed of two active components of Mn containing metal–organic framework (MOF) shell, [ImH][$Mn(BTC)(H_2O)$], and $Zn_{0.4}Fe_{2.6}O_4$ magnetic nanoparticle (MNP) core (Figure 2a).[23,24] Mn is chosen as a T_1 contrast component because it has unpaired d-electrons which are effective for faster T_1 relaxation. Importantly, Mn is an alternative biocompatible candidate to lanthanide metals (*e.g.*, Gd) which cause harmful side effects such as nephrogenic systemic fibrosis (NSF).[25] MNP with high saturation magnetization value (M_s) of 161 emu g^{-1} provides large magnetic field for faster T_2 relaxation.[23] The core–shell structure of mAFIA is shown in the transmission electron microscope (TEM) image and electron energy loss spectrum (EELS) mapped image where Fe at the core, Si at the separating layer, and Mn at the shell are coded with yellow, brown, and green, respectively (Figure 2b). The synthesized mAFIA is stably dispersed in aqueous solution, maintaining its initial hydrodynamic size for over a week (see Supporting Information Figure S1).

The contrast effects of mAFIA are evaluated by comparing its MRI signals with those of conventional contrast agents (Magnevist and Feridex) and deionized water (DIW). As shown in Figure 2c,d, mAFIA shows

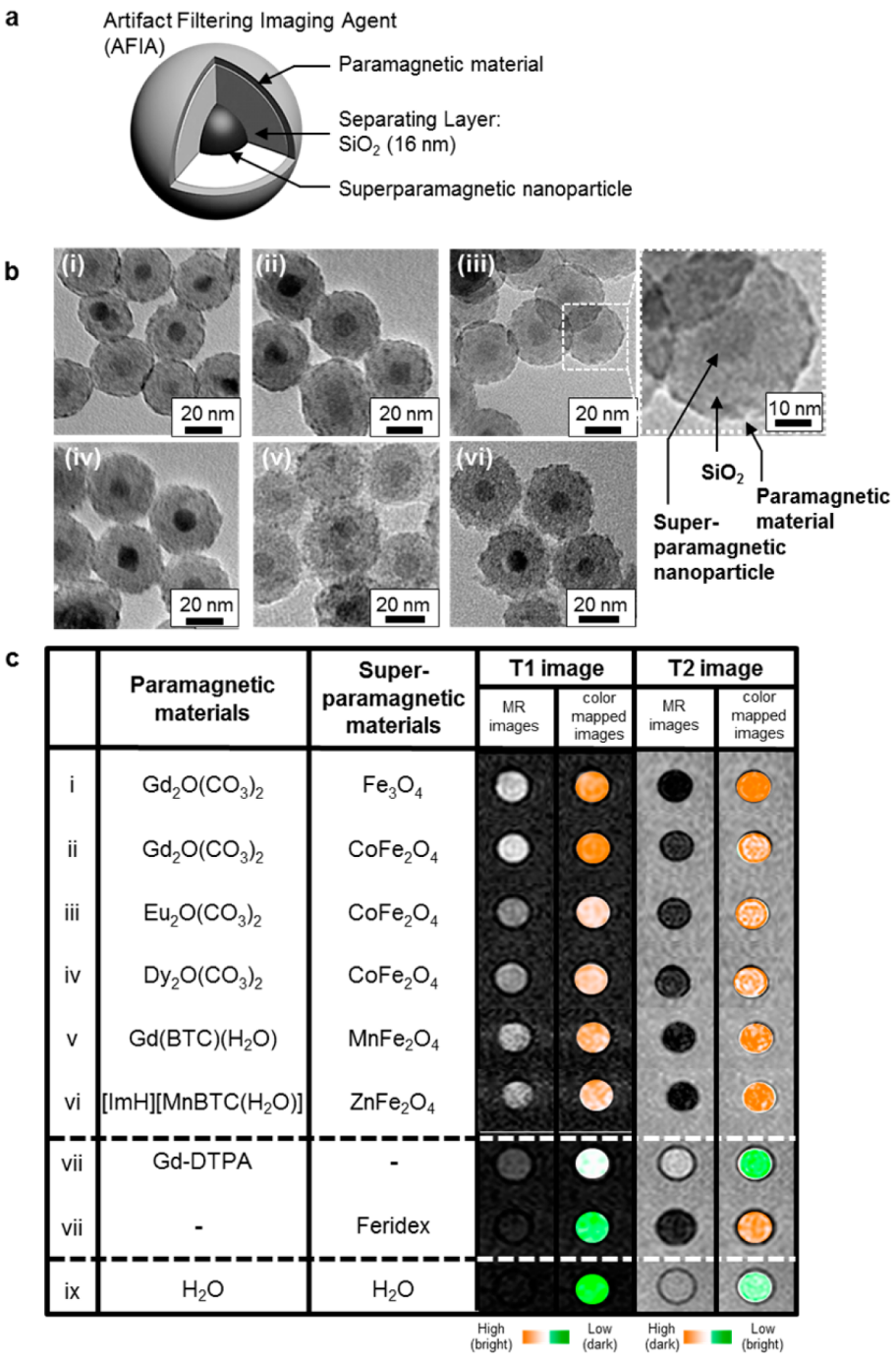

Figure 1. Variety of AFIAs and their MRI contrast effects. (a) Schematic illustration of core–shell structured AFIA. (b) TEM images of various core–shell structured AFIAs including Fe_3O_4@SiO_2@$Gd_2O(CO_3)_2$ (i), $CoFe_2O_4$@SiO_2@$Gd_2O(CO_3)_2$ (ii), $CoFe_2O_4$@SiO_2@$Eu_2O(CO_3)_2$ (iii), $CoFe_2O_4$@SiO_2@$Dy_2O(CO_3)_2$ (iv), $MnFe_2O_4$@SiO_2@Gd(BTC)(H_2O) (v), and $ZnFe_2O_4$@SiO_2@[ImH][Mn(BTC)(H_2O)] (vi). Thickness of separating layer (SiO_2) is fixed at 16 nm. Magnified TEM image of $CoFe_2O_4$@SiO_2@$Eu_2O(CO_3)_2$ (white dotted box) shows the core–shell structure of the AFIA. (c) MRI images and their color-coded images of AFIAs and conventional contrast agents. Fe_3O_4@SiO_2@$Gd_2O(CO_3)_2$ (i), $CoFe_2O_4$@SiO_2@$Gd_2O(CO_3)_2$ (ii), $CoFe_2O_4$@SiO_2@$Eu_2O(CO_3)_2$ (iii), $CoFe_2O_4$@SiO_2@$Dy_2O(CO_3)_2$ (iv), $MnFe_2O_4$@SiO_2@Gd(BTC)(H_2O) (v), $ZnFe_2O_4$@SiO_2@[ImH][Mn(BTC)(H_2O)] (vi), Gd-DTPA (vii), Feridex (viii), and H_2O (ix). Images of contrast agents are taken by using 3.0 T MRI at the identical metal concentrations.

large MRI contrast enhancements in both T_1 and T_2 images, which appear as a brighter signal in the T_1 image and a darker signal in the T_2 image compared to those of water. On the other hand, Magnevist and Feridex display high contrast effects only in T_1 or T_2 images, respectively. Moreover, the mAFIA has more than two times higher T_1 and T_2 relaxivity coefficients ($r_1 = 8.2\ mM^{-1}\ s^{-1}$, $r_2 = 238.4\ mM^{-1}\ s^{-1}$) than Magnevist ($r_1 = 3.8\ mM^{-1}\ s^{-1}$) and Feridex ($r_2 = 109.4\ mM^{-1}\ s^{-1}$) (Figure 2e,f). These relaxivity coefficients of mAFIA are

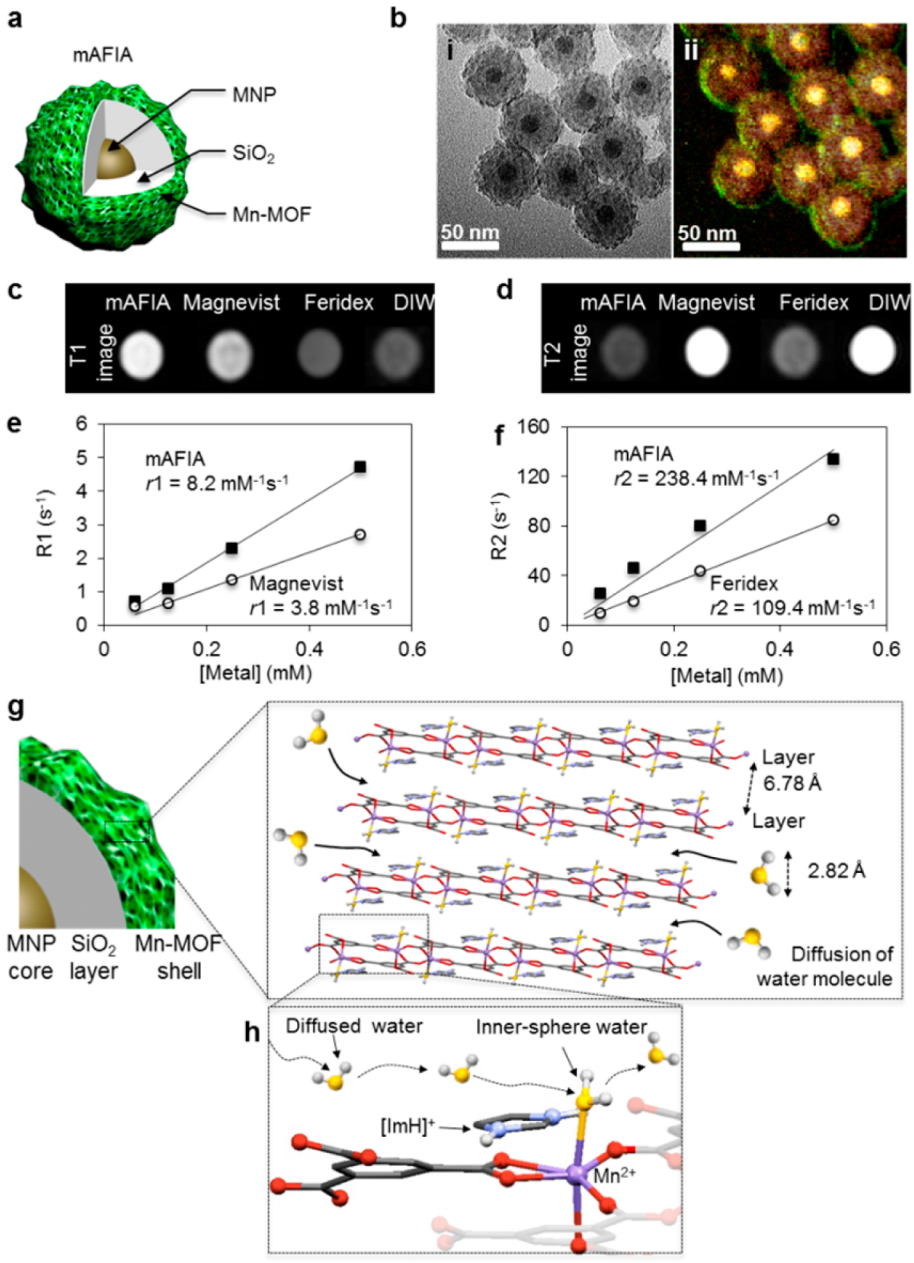

Figure 2. mAFIA and its MRI contrast effects. (a) mAFIA is comprises a $Zn_{0.4}Fe_{2.6}O_4$ magnetic nanoparticle (MNP) core, a SiO_2 separating layer, and a Mn-MOF shell. (b) TEM image of the mAFIA with an average size of 50 nm (i). EELS analysis of mAFIA in which Fe, Si, and Mn are coded with yellow, brown, and green, respectively (ii). (c) T_1 and (d) T_2 images of the mAFIA, Magnevist, and Feridex obtained by using 3.0 T MRI. The concentration of contrast agents used in T_1 and T_2 images are 0.5 mM (metal) and 0.25 mM (metal), respectively. The mAFIA shows strong MRI contrast effects in both the T_1 and T_2 images. (e,f) Plots of R_1 (R_2) *vs* concentration of the metal; r_1 and r_2 of mAFIA are ~2-fold larger than those of conventional contrast agents. (g) Two-dimensional layer structure of the shell of the mAFIA, [ImH][Mn(BTC)(H_2O)]. The anionic 2-D layer ([Mn(BTC)(H_2O)]$^-$) is stabilized by charge compensator, protonated imidazole ([ImH]$^+$). Water can approach to the paramagnetic metal center by diffusing through space between two layers. (h) Mn^{2+} ion is octahedrally coordinated by five oxygen atoms and one inner-sphere water, which is directly bonded to metal. Exchange of inner-sphere water molecule with a diffused water molecule can contribute to T_1 relaxation enhancement.

remarkable since its r_1 value is larger than those of reported manganese-based contrast agents (see Supporting Information Table S1) and is even comparable to Gd-based contrast agent (*e.g.*, Magnevist). By virtue of high sensitivities of mAFIA, it shows high MRI signals in both T_1 and T_2 images when the concentration is in the range of 0.03125 to 0.5 mM (see Supporting Information Figure S2). Such high sensitivities of mAFIA are beneficial for AND logic gate processing.

The strong T_1 contrast effects of mAFIA are largely caused by the structural advantages of the MOF,[26,27] especially those associated with the 2-D layered [ImH][Mn(BTC)(H_2O)] (Figure 2g). The Mn^{2+} ion is

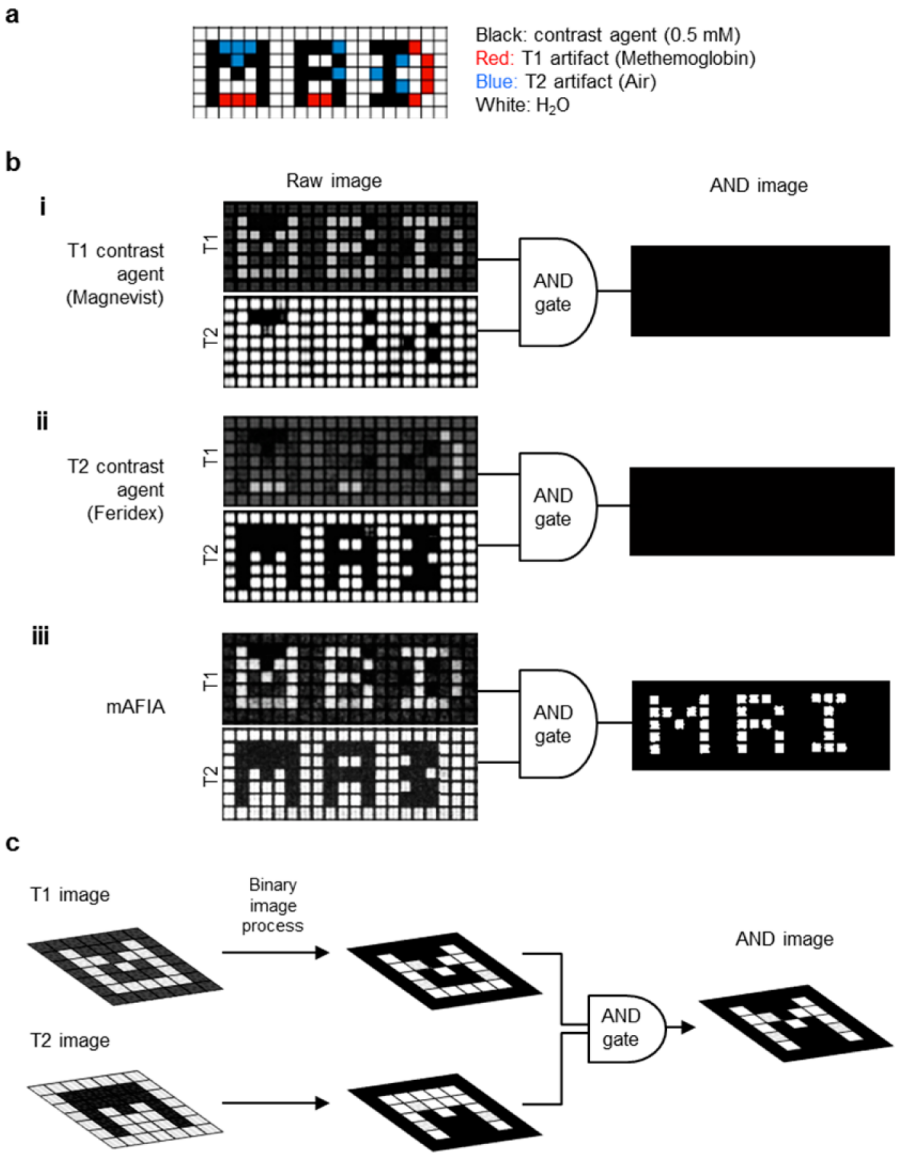

Figure 3. Artifact filtering scheme of the mAFIA. (a) Design of phantom containing contrast agents and artifact materials. In the well plates, contrast agent (Magnevist or Feridex or mAFIA) and artifacts (methemoglobin, air) are filled in each of the wells. (b) T_1 and T_2 images of phantoms are post processed using the AND logic algorithm. In the AND image, no signal is observed when conventional T_1 and T_2 contrast agents are utilized (i, ii). The characters "MRI" are obtained only using the mAFIA followed by conducting AND logic gate process (iii). (c) Schematic description of image processing and AND logic algorithm. Regions showing higher signal than the threshold (signal of water) are selected and marked with a white color. Then, both images are passed through an AND gate. Only the regions of high MRI signal in both T_1 and T_2 images yield a valid AND logic output, and the rest of them are considered as meaningless.

octahedrally coordinated by five oxygen atoms from trimesates (BTC^{3-}) and one inner-sphere water molecule, forming $[Mn(BTC)(H_2O)]^-$ (Figure 2h). A protonated imidazole (ImH^+), a charge compensator, is located between 2-D layers (Figure 2g,h). The interlayer distance of 6.78 Å can make water molecules (2.82 Å) have easy access to magnetic metal ions (Mn^{2+}) inside of the MOF (Figure 2g), where they can effectively undergo exchange with the inner-sphere water molecule (Figure 2h).[26,28]

Artifact Filtering Capability of mAFIA. By virtue of high MRI T_1 and T_2 contrast effects, mAFIA is capable of performing AND logic gate process, which gives meaningful output only if both input MRI signals of T_1 and T_2 are simultaneously high. To demonstrate that the mAFIA can filter out various false signals (artifacts) *via* AND logic gate process, MRI phantom plates filled with contrast agents and artifacts are designed and imaged with 3.0 T MRI. As shown in Figure 3a, each well is filled with the following materials: (i) black wells, different type of contrast agent (Magnevist, Feridex, or mAFIA); (ii) red wells, methemoglobin (T_1 artifact); (iii) blue wells, air (T_2 artifact); and (iv) white wells, water. In phantom containing Magnevist, the characters, "MRI", are observed as bright signals in the T_1 image and irregular dark spots are shown in the T2 image (Figure 3b(i)). In the phantom containing Feridex, the

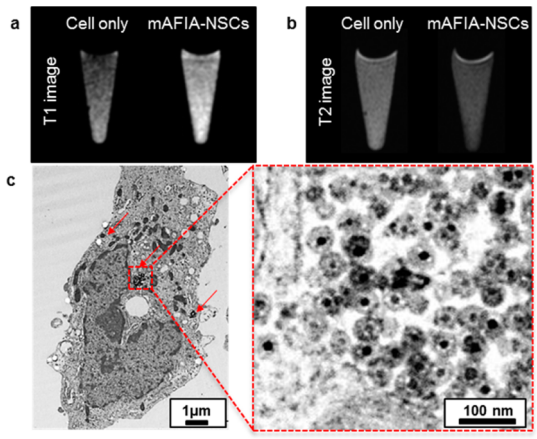

Figure 4. Labeling of human neural stem cells (NSCs) with the mAFIA. (a) T_1 and (b) T_2 images of unlabeled control NSCs and mAFIA-labeled NSCs (mAFIA-NSCs). mAFIA-NSCs show high MRI signal compared to control group (cell only) in both of T_1 and T_2 images. (c) TEM images of the mAFIA-NSC. The internalized mAFIA is located at the endosomes of the NSC (indicated by red arrows) and has a preserved core−shell structure (enlarged TEM image, red dotted box).

characters, "MRI", are observed as dark signals in the T_2 image along with irregular spots of bright signals in the T_1 image (Figure 3b(ii)). In the case of phantom containing mAFIA, "UCLA" and "MRI" are clearly observed in the T_1 and T_2 images, respectively (Figure 3b(iii)). When these images are postprocessed utilizing an AND logic algorithm, all of the artifacts are filtered out and only areas showing high MRI contrast enhancements in both T_1 and T_2 images exhibit AND logic output (Figure 3c). Therefore, only mAFIA is confirmed to have image of "MRI" by filtering out intentionally inserted T_1 and T_2 artifacts, while the other contrast agents cannot.

MRI Stem Cell Tracking Using mAFIA. As a model case, we test the mAFIA for *in vivo* MRI tracking of stem cell. In typical MRI stem cell tracking studies, cells are transfected with MRI contrast agent and monitored indirectly through the signal of contrast agent.[29,30] However, the difficulty of distinguishing contrast agent from artifacts still remains a challenging obstacle to investigate the behavior of transplanted stem cells *in vivo*. To address this issue, we first transfect human neural stem cells (NSCs) with the mAFIA and obtain *in vitro* MRI images. Samples for MRI imaging are prepared by fixing and dispersing respective mAFIA-NSCs and unlabeled control NSCs in 0.1 wt % agarose gel and by solidifying them. Compared to unlabeled control NSCs, mAFIA-labeled NSCs (mAFIA-NSCs) clearly show brighter and darker signal in respective T_1 and T_2 images (Figure 4a,b). The TEM images of the mAFIA-NSCs show that the mAFIA is located at the endosomes of the NSCs and retains its core−shell structure (Figure 4c). The biocompatibility of mAFIA is examined with TUNEL assay and caspase-3 activity assay. According to results, no difference in cell viability is observed between mAFIA-NSCs and unlabeled control NSCs, indicating that mAFIA has no cytotoxicity on NSCs (see Supporting Information Figure S3).

Next, we investigate the new imaging agent in rat brain stroke model, where such injury is known to promote neural stem cell migration toward the infarcted area.[31] In MRI images of rat before inducing cerebral infarction (Figure 5a,b), several brain tissues show their inherent contrasts (*e.g.*, ventricle, bright in the T2 image, dark in the T_1 image; corpus callosum, dark in the T_2 image). After induction of infarction, the infarcted area is clearly shown as bright signal in the T_2 image mostly in right cerebral hemisphere (Figure 5c), although it is hardly pronounced in the T_1 image (Figure 5d). This is consistent with the fact that cerebral infarction gives a bright signal in the T_2 image but produces negligible contrast change at an early stage in the T_1 image.[32] mAFIA-NSCs are then injected into the right corpus callosum of the rat brain 3 days after induction of right focal cerebral infarction (Figure 5c,d). At day 0 after injection, mAFIA-NSCs are observed at the injection site (red box) as strong dark signals in both the T_2 and T_1 images (Figure 5c,d). The presence of a dark signal surrounded by a bright circle in the T_1 image (Figure 5d) is caused by the high concentrations of the mAFIA-NSCs at the injection site, which is a known phenomenon associated with T_1 contrast agents that cause local magnetic field distortion at high concentration (see Supporting Information Figure S4).[21,33−36]

At day 14 after mAFIA-NSCs injection, in the case of the T_2 image, although the entire infarcted area is shown as a bright signal in the right hemisphere of rat brain (Figure 5e), a number of dark spots are observed not only at the injection site (red box) but also at other sites (blue arrows) around the infarcted area, between both left and right ventricles, beside the left ventricle, and the left cerebral hemisphere. In the T_1 image (Figure 5f), spots of bright signals are shown nearby the mAFIA-NSCs' injection site (red box) and also at other sites around the infarcted area (blue arrows). Different distribution patterns and discrepancies of MRI signals between the T_2 and T_1 images, partly caused by conditions created by the brain infarction, lead to ambiguities in determining the location of the stem cells (*i.e.*, mAFIA-NSCs).

Here, we take advantage of the artifact filtering capability of mAFIA and the AND logic gate process. Because the signal darkening effects in the T_1 image is limited only at the injection site, it does not hinder the determination of the exact location of migrated stem cells *via* AND logic gate process. First, the T_2 and T_1 images are color-coded with respect to signal intensities (Figure 5g,h), with orange (high signal intensity) and green color (low signal intensity). Then, both images are postprocessed with the AND logic algorithm (see Supporting Information). AND logic output (orange, Figure 5i) shows the areas having strong MRI signals in both the T_2 and T_1 images. Those areas

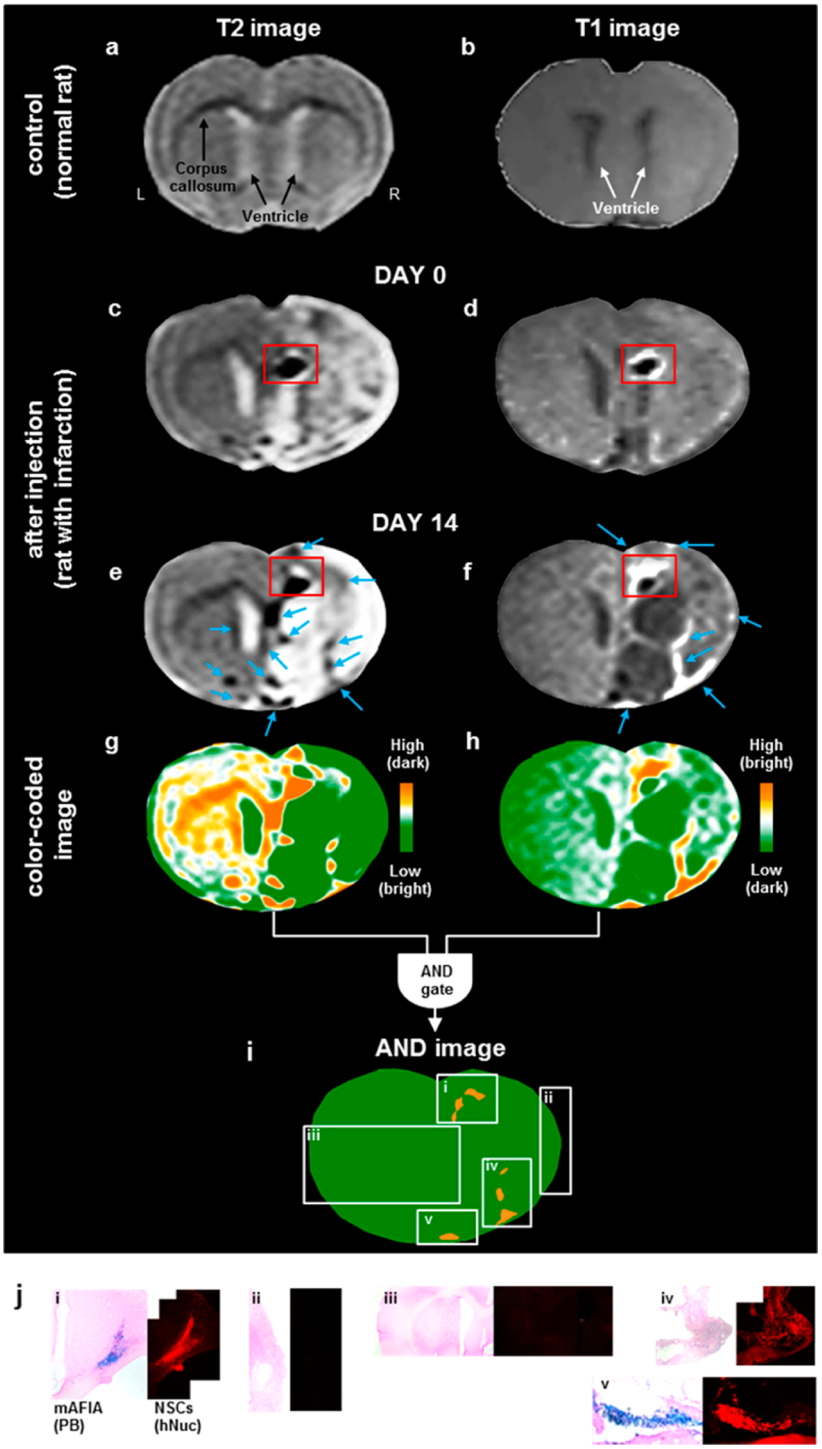

Figure 5. *In vivo* MRI tracking of NSCs using the mAFIA. (a,b) MRI images of rat brain before inducing infarction. Characteristic MRI signals of ventricle (bright in the T_2 image, dark in the T_1 image) and corpus callosum (dark in the T_2 image) are observed. (c,d) MRI images of infarcted brain obtained at day 0 immediately after mAFIA-NSC injection. (c) Strong dark signal caused by mAFIA-NSCs is observed at the injection site (red box) in the T_2 image. The bright signal caused by infarction is observed over broad ranges of the right hemisphere. (d) Dark signal surrounded by a bright circle from mAFIA-NSCs (red box) is shown in the T_1 image. (e,f) At day 14, infarction has severely progressed. The initial injection site is marked with the red box, and newly appearing regions of high MRI signal are indicated by blue arrows. (g,h) Orange color in the color-coded images shows the regions of high MRI signal. (i) AND logic output (orange) in the AND image is observed in the vicinity of the (i) injection site, (iv) external capsule and piriform cortex, and (v) olfactory tubercle (white boxes). (j) Reliability of the AND image is verified by using a histological study. In the dissected brain, mAFIA is stained by using Prussian blue (PB, blue) and NSCs are stained by using hNuc (red). The location of the mAFIA and NSCs well match those indicated by the distribution of the AND logic output (i, iv, v). No blue or red staining is detected in regions where no AND logic output is observed (ii, iii).

are the location of stem cells (*i.e.*, mAFIA-NSCs), which appear near the vicinity of the injection site (Figure 5i(i)), bottom right portion of brain (external capsule and piriform cortex, Figure 5i(iv)), and bottom middle region of brain (olfactory tubercle, Figure 5i(v)). To confirm the reliability of the AND image, a histology study is performed (Figure 5j(i–v) in which the mAFIA is stained by using Prussian blue (PB, blue) and NSCs are stained with the anti-human nuclei marker (hNuc, red). In the image of the dissected rat brain at day 14, the areas having the AND logic output (Figure 5j(i,iv,v) show blue and red colors, confirming the existence of the mAFIA and NSCs. In contrast, regions with either high T_1 (Figure 5j(ii)) or T_2 signal (Figure 5j(iii)) do not display blue or red color, indicating that stem cells or the contrast agent are not present at these locations. The AND image obtained after AND logic gate process shows the locations of stem cells which are migrated from their initial injection site toward the proximity of infarcted areas (lower right and bottom portion of brain) at 14 days after the injection.

CONCLUSIONS

In summary, we report the design concept and its generalization of artifact filtering imaging agent (AFIA) *via* simple and reproducible synthetic methods. By introducing Mn-MOF, which has advantages of efficient water exchange, it is possible to achieve biocompatible AFIA which has high T_1 contrast effects surpassing those of various Mn-based contrast agents. Then, we demonstrate that a combination of the AFIA and AND logic algorithm can be an effective tool for MRI artifact elimination, which has been a difficult task. The potential applicability of AFIA is ample and, for example, can be useful as a new tool to accurately image early stage tumor, vascular system, stem cell, or central nervous system, in which numerous artifacts are undermining accurate diagnosis.

METHODS

Synthesis of AFIA. The core superparamagnetic nanoparticles were synthesized by using the reported one-pot thermal decomposition method.[23] Core@SiO_2 nanoparticles with a 16 nm SiO_2 shell were synthesized by using a base-catalyzed sol–gel reaction.[22,37] Paramagnetic shell was grown on the surface of the carboxylic acid functionalized silica shell *via* reduction or self-assembly of metal precursors and ligands. The detailed procedures are described in Supporting Information.

AND Logic Algorithm. MRI images in Figure 3 and Figure 5 were processed with the AND logic algorithm by using MATLAB (version 7.10 (R2010a), Mathworks, USA). The detailed algorithm is described in Supporting Information.

Measurements of r_1 and r_2 of Various Contrast Agents. The r_1 and r_2 values of contrast agents were measured using a 1.5 T MRI (Philips, Germany). r_1 was measured by using various inversion times (TI) with the following inversion recovery sequence: TI = 100, 500, 1000, 2000, and 3000 ms, echo time (TE) = 7.4 ms, FOV = 100 mm, matrix = 256 × 256, slice thickness = 2 mm, and acquisition number = 1. r_2 was measured by using a Carr–Purcell–Meiboom–Gill (CPMG) sequence: repetition time (TR) = 5000 ms, TE = 10 to 1280 ms, FOV = 100 mm, matrix = 256 × 256, slice thickness = 2 mm, and acquisition number = 1.

MRI Imaging. MRI imaging of AFIA solutions and rat brains were performed by using a 3.0 T MRI (Achieva XT, Philips, The Netherlands) with an animal coil (Shanghai Chenguang). T_1 images were determined using the following sequence: TR = 625 ms, TE = 10 ms, FOV = 75 mm, matrix = 256 × 256, slice thickness = 0.7 mm, acquisition number = 1. T_2 images were obtained by using the following fast spin–echo sequence: TR = 4000 ms, TE = 80 ms, FOV = 75 mm, matrix = 256 × 256, slice thickness = 0.7 mm, acquisition number = 1.

***In Vitro* Experiments.** NSCs were originally derived from the telencephalon of an aborted fetal brain at 13 weeks of gestation. For the labeling of NSCs with mAFIA, poly-L-lysine (PLL) was combined with mAFIA, and the mAFIA-PLL complex was allowed to incubate for 48 h. More details about NSC labeling and sample preparation for TEM and MRI analyses are described in Supporting Information.

Animal Experiments. Adult male Sprague-Dawley rats weighing 250–300 g were maintained in accordance with the guidelines and under approval of the Animal Care Committee of Yonsei University. The detailed procedures for MCAO rat model preparation and histological studies are described in Supporting Information.

Conflict of Interest: The authors declare no competing financial interest.

Acknowledgment. We thank J.K. Kim (KBSI) for HVEM analyses, and S. Lee (Yonsei University) for programming the algorithm used for the AND logic gate process. The authors especially appreciate Dr. D. Yoo for helpful discussions. This work was financially supported by the National Creative Research Initiatives Program (2010-0018286 to J.C.), Korea Healthcare Technology R&D Project, Ministry for Health & Welfare Affairs (HI08C2149 to J.C.), National Research Foundation (NRF; 2010-0020289, 2013M3A9B4076545 to K.I.P.), Korean Health Technology R&D Project (A091159, A121943 to K.I.P.), and Basic Science Research Program through the NRF (2010-0013568 to H.S., 2011-0008018 to Y.K.).

Supporting Information Available: Details about AFIA preparation, shell materials structure analyses, AND logic algorithm, *in vitro* and *in vivo* experiments. MRI relaxivity coefficients of various MRI contrast agents. MRI data showing correlation between *in vitro* MRI signal intensity and concentrations of cells. This material is available free of charge *via* the Internet at http://pubs.acs.org.

REFERENCES AND NOTES

1. Sun, C.; Lee, J. S. H.; Zhang, M. Magnetic Nanoparticles in MR Imaging and Drug Delivery. *Adv. Drug Deliv. Rev.* **2008**, *60*, 1252–1265.
2. Xu, C.; Xie, J.; Ho, D.; Wang, C.; Kohler, N.; Walsh, E. G.; Morgan, J. R.; Chin, E.; Sun, S. Au–Fe_3O_4 Dumbbell Nanoparticles as Dual-Functional Probes. *Angew. Chem., Int. Ed.* **2007**, *47*, 173–176.
3. Liu, Z.; Cai, W.; He, L.; Nakayama, N.; Chen, K.; Sun, X.; Chen, X.; Dai, H. *In Vivo* Biodistribution and Highly Efficient Tumour Targeting of Carbon Nanotubes in Mice. *Nat. Nanotechnol.* **2007**, *2*, 47–52.
4. Yoon, T.-J.; Lee, H.; Shao, H.; Weissleder, R. Highly Magnetic Core–Shell Nanoparticles with a Unique Magnetization Mechanism. *Angew. Chem., Int. Ed.* **2011**, *50*, 4663–4666.
5. Medintz, I. L.; Uyeda, H. T.; Goldman, E. R.; Mattoussi, H. Quantum Dot Bioconjugates for Imaging, Labelling and Sensing. *Nat. Mater.* **2005**, *4*, 435–446.
6. Gao, J.; Gu, H.; Xu, B. Multifunctional Magnetic Nanoparticles: Design, Synthesis, and Biomedical Applications. *Acc. Chem. Res.* **2009**, *42*, 1097–1107.

7. Cai, W.; Shin, D.-W.; Chen, K.; Gheysens, O.; Cao, Q.; Wang, S. X.; Gambhir, S. S.; Chen, X. Peptide-Labeled Near-Infrared Quantum Dots for Imaging Tumor Vasculature in Living Subjects. *Nano Lett.* **2006**, *6*, 669–676.
8. Hu, M.; Chen, J.; Li, Z.-Y.; Au, L.; Hartland, G. V.; Li, X.; Marquez, M.; Xia, Y. Gold Nanostructures: Engineering Their Plasmonic Properties for Biomedical Applications. *Chem. Soc. Rev.* **2006**, *35*, 1084–1094.
9. Nasongkla, N.; Bey, E.; Ren, J.; Ai, H.; Khemtong, C.; Guthi, J. S.; Chin, S.-F.; Sherry, A. D.; Boothman, D. A.; Gao, J. Multifunctional Polymeric Micelles as Cancer-Targeted, MRI-Ultrasensitive Drug Delivery Systems. *Nano Lett.* **2006**, *6*, 2427–2430.
10. Weissleder, R.; Moore, A.; Mahmood, U.; Bhorade, R.; Benveniste, H.; Chiocca, E. A.; Basilion, J. P. *In Vivo* Magnetic Resonance Imaging of Transgene Expression. *Nat. Med.* **2000**, *6*, 351–355.
11. Weissleder, R.; Mahmood, U. Molecular Imaging. *Radiology* **2001**, *219*, 316–333.
12. Brown, M. A.; Semelka, R. C. *MRI: Basic Principles and Applications*; Wiley-Liss: New York, 2003.
13. Na, H. B.; Song, I. C.; Hyeon, T. Inorganic Nanoparticles for MRI Contrast Agents. *Adv. Mater.* **2009**, *21*, 2133–2148.
14. Hamer, O. W.; Schlottmann, K.; Sirlin, C. B.; Feuerbach, S. Technology Insight: Advances in Liver Imaging. *Nat. Rev. Gastroenterol. Hepatol.* **2007**, *4*, 215–228.
15. Ahmed, H. U.; Kirkham, A.; Arya, M.; Illing, R.; Freeman, A.; Allen, C.; Emberton, M. Is it Time To Consider a Role for MRI before Prostate Biopsy? *Nat. Rev. Clin. Oncol.* **2009**, *6*, 197–206.
16. Bulte, J. W. M.; Kraitchman, D. L. Iron Oxide MR Contrast Agents for Molecular and Cellular Imaging. *NMR Biomed.* **2004**, *17*, 484–499.
17. Liu, W.; Dahnke, H.; Jordan, E. K.; Schaeffter, T.; Frank, J. A. *In Vivo* MRI Using Positive-Contrast Techniques in Detection of Cells Labeled with Superparamagnetic Iron Oxide Nanoparticles. *NMR Biomed.* **2008**, *21*, 242–250.
18. Helms, C. A. The Use of Fat Suppression in Gadolinium-Enhanced MR Imaging of the Musculoskeletal System: A Potential Source of Error. *Am. J. Roentgenol.* **1999**, *173*, 234–236.
19. Seo, W. S.; Lee, J. H.; Sun, X.; Suzuki, Y.; Mann, D.; Liu, Z.; Terashima, M.; Yang, P. C.; McConnell, M. V.; Nishimura, D. G.; *et al.* FeCo/Graphitic-Shell Nanocrystals as Advanced Magnetic-Resonance-Imaging and Near-Infrared Agents. *Nat. Mater.* **2006**, *5*, 971–976.
20. Richard, C.; Doan, B.-T.; Beloeil, J.-C.; Bessodes, M.; Tóth, E.; Scherman, D. Noncovalent Functionalization of Carbon Nanotubes with Amphiphilic Gd^{3+} Chelates: Toward Powerful T_1 and T_2 MRI Contrast Agents. *Nano Lett.* **2008**, *8*, 232–236.
21. Shin, J.; Anisur, R. M.; Ko, M. K.; Im, G. H.; Lee, J. H.; Lee, I. S. Hollow Manganese Oxide Nanoparticles as Multifunctional Agents for Magnetic Resonance Imaging and Drug Delivery. *Angew. Chem., Int. Ed.* **2009**, *48*, 321–324.
22. Choi, J.-s.; Lee, J.-H.; Shin, T.-H.; Song, H.-T.; Kim, E. Y.; Cheon, J. Self-Confirming "AND" Logic Nanoparticles for Fault-Free MRI. *J. Am. Chem. Soc.* **2010**, *132*, 11015–11017.
23. Jang, J.-t.; Nah, H.; Lee, J.-H.; Moon, S. H.; Kim, M. G.; Cheon, J. Critical Enhancements of MRI Contrast and Hyperthermic Effects by Dopant-Controlled Magnetic Nanoparticles. *Angew. Chem., Int. Ed.* **2009**, *48*, 1234–1238.
24. Mahata, P.; Natarajan, S. The First Observation of a Na_2TiS_2 Related Structure in a 2-D Anionic Manganese Trimesate Intercalated by Cationic Imidazole. *CrystEngComm.* **2009**, *11*, 560–563.
25. Penfield, J. G.; Reilly, R. F., Jr. What Nephrologists Need To Know about Gadolinium. *Nat. Clin. Pract. Nephrol.* **2007**, *3*, 654–668.
26. Horcajada, P.; Chalati, T.; Serre, C.; Gillet, B.; Sebrie, C.; Baati, T.; Eubank, J. F.; Heurtaux, D.; Clayette, P.; Kreuz, C.; *et al.* Porous Metal-Organic-Framework Nanoscale Carriers as a Potential Platform for Drug Delivery and Imaging. *Nat. Mater.* **2010**, *9*, 172–178.
27. Rocca, J. D.; Liu, D.; Lin, W. Nanoscale Metal–Organic Frameworks for Biomedical Imaging and Drug Delivery. *Acc. Chem. Res.* **2011**, *44*, 957–968.
28. Acik, M.; Mattevi, C.; Gong, C.; Lee, G.; Cho, K.; Chhowalla, M.; Chabal, Y. J. The Role of Intercalated Water in Multilayered Graphene Oxide. *ACS Nano* **2010**, *4*, 5861–5868.
29. Lewin, M.; Carlesso, N.; Tung, C. H.; Tang, X. W.; Cory, D.; Scadden, D. T.; Weissleder, R. Tat Peptide-Derivatized Magnetic Nanoparticles Allow *In Vivo* Tracking and Recovery of Progenitor Cells. *Nat. Biotechnol.* **2000**, *18*, 410–414.
30. Rogers, W. J.; Meyer, C. H.; Kramer, C. M. Technology Insight: *In Vivo* Cell Tracking by Use of MRI. *Nat. Clin. Pract. Cardiovasc. Med.* **2006**, *3*, 554–562.
31. Imitola, J.; Raddassi, K.; Park, K. I.; Mueller, F.-J.; Nieto, M.; Teng, Y. D.; Frenkel, D.; Li, J.; Sidman, R. L.; Walsh, C. A.; *et al.* Directed Migration of Neural Stem Cells to Sites of CNS Injury by the Stromal Cell-Derived Factor 1α/CXC Chemokine Receptor 4 Pathway. *Proc. Natl. Acad. Sci. U.S.A.* **2004**, *101*, 18117–18122.
32. Culebras, A.; Kase, C. S.; Masdeu, J. C.; Fox, A. J.; Bryan, R. N.; Grossman, C. B.; Lee, D. H.; Adams, H. P.; Thies, W. Practice Guidelines for the Use of Imaging in Transient Ischemic Attacks and Acute Stroke. *Stroke* **1997**, *28*, 1480–1497.
33. McRobbie, D. W.; Moore, E. A.; Graves, M. J.; Prince, M. R. *MRI from Picture to Proton*; Cambridge University Press: Cambridge, UK, 2003.
34. Cha, S.; Knopp, E. A.; Johnson, G.; Wetzel, S. G.; Litt, A. W.; Zagzag, D. Intracranial Mass Lesions: Dynamic Contrast-Enhanced Susceptibility-Weighted Echo-Planar Perfusion MR Imaging. *Radiology* **2002**, *223*, 11–29.
35. May, D. A.; Pennington, D. J. Effect of Gadolinium Concentration on Renal Signal Intensity: An *In Vitro* Study with a Saline Bag Model. *Radiology* **2000**, *216*, 232–236.
36. Masi, J. N.; Newitt, D.; Sell, C. A.; Daldrup-Link, H.; Steinbach, L.; Majumdar, S.; Link, T. M. Optimization of Gadodiamide Concentration for MR Arthrography at 3 T. *Am. J. Roentgenol.* **2005**, *184*, 1754–1761.
37. Yi, D. K.; Lee, S. S.; Papaefthymiou, G. C.; Ying, J. Y. Nanoparticle Architectures Templated by SiO_2/Fe_2O_3 Nanocomposites. *Chem. Mater.* **2006**, *18*, 614–619.